

An efficient PSF construction method

M. Gai¹ ^{*} and R. Cancelliere²

¹*Istituto Nazionale di Astrofisica - Osservatorio Astronomico di Torino, V. Osservatorio 20, 10025 Pino T.se (TO), Italy*

²*Dipartimento di Informatica, Università di Torino, C.so Svizzera 185, 10149 Torino, Italy*

Accepted 2007 March 1. Received 2007 March 1; in original form 2006 December 18

ABSTRACT

Image computation is a fundamental tool for performance assessment of astronomical instrumentation, usually implemented by Fourier transform techniques. We review the numerical implementation, evaluating a direct implementation of the discrete Fourier transform (DFT) algorithm, compared with fast Fourier transform (FFT) tools. Simulations show that the precision is quite comparable, but in the case investigated the computing performance is considerably higher for DFT than FFT. The application to image simulation for the mission Gaia and for Extremely Large Telescopes is discussed.

Key words: telescopes – methods: numerical – instrumentation: miscellaneous.

1 INTRODUCTION

The imaging performance of astronomical instruments, and optical instrumentation in general, is related to the Point Spread Function (PSF), i.e. the intensity distribution from a point-like object at infinity, which is in most cases a satisfactory representation of a star. The monochromatic PSF is computed as square modulus of the field amplitude on the focal plane; the amplitude function, in turn, is built through the diffraction integral, derived from the wave description of electromagnetic radiation. An historical review of the diffraction theory is out of the scope of this paper, devoted to performance comparison of two Fourier transform (FT) algorithms computing the diffraction integral.

The PSF includes, by a suitable wavefront description, details of the instrumental response. The polychromatic PSF of an unresolved star is produced by superposition, weighed by spectral distribution, of the monochromatic PSFs; thus, objects with different spectral characteristics have different polychromatic PSF. The image of a resolved source can be described as a superposition of PSFs, weighed by spectrum and spatial distribution. The response of a spectrograph can be built in quite the same way, apart the explicit wavelength dependence of the monochromatic PSF location. PSF construction is therefore a quite general tool.

An accurate PSF description for an optical instrument, either in design or observation phase (through calibration), is crucial to any astrophysical measurement. In the former case, system parameters are tuned to improve the performance, whereas in the latter the instrument signature must be identified for measurements correction and determination of the intrinsic objects characteristics.

The PSF is usually computed numerically, although useful

analytical approximations are derived e.g. in Braat (2002). The FFT is used for PSF construction also by professional ray tracing packages (e.g. Zemax or Code V).

We discuss the numerical implementation of the FT, through a method of direct computation which, under appropriate conditions, may be more convenient than the usual Fast Fourier Transform (FFT) tools. The computing time required by the proposed PSF construction method is significantly lower than the equivalent FFT case; also, the result precision can be higher, since the generation of some artefacts is suppressed. Both aspects are relevant to applications, with benefits on processing, resolution and/or precision.

In most of our simulations, the case study is the telescope of the Gaia mission (Perryman et al. 2001), approved by the European Space Agency for launch in 2011, and aimed at a high precision astrometric survey of our Galaxy. The science data simulations require high accuracy, for proper validation of the reduction algorithms under development by the astrophysical community involved. A specific application to wavelength dependence, already dealt with by the authors (Gai and Cancelliere 2005), is further developed in Cancelliere and Gai (2007), recently submitted. We also mention the possible application of the proposed PSF construction method to the case of Extremely Large Telescopes, which among other technological challenges also feature impressive numerical requirements.

In section 2 we recall the basics of the diffraction integral and discuss its key implementation features. In section 3 we compare some of the more relevant features of FFT and DFT implementations, in terms of processing time and accuracy. Then, in section 4, we discuss the PSF dependence from wavelength and the possible introduction of artefacts. In section 5 we assess the application of the proposed method to modern Extremely Large Telescopes. Finally, we draw our conclusions.

* E-mail: gai@oato.inaf.it (MG), cancelli@di.unito.it (RC)

2 THE DIFFRACTION INTEGRAL

The definitions related to imaging performance derive from a wide range of applications; hereafter, we mostly follow the notation from Born and Wolf (1985).

A point-like source at infinity, as can be considered a star except for very high spatial resolution instruments (like interferometers), generates a spherical wavefront which can be considered flat at the entrance of a telescope. This description neglects the disturbances in the medium, e.g. air turbulence; in modern ground based telescopes, an Adaptive Optics (AO) system is used to recover, at least in part, the ideal diffraction limited performance.

The telescope, ideally, folds the input wavefront towards a single point of the focal plane (FP), where the diffraction image is achieved. The imaging performance of a real optical system can usually be described by the discrepancy with respect to ideal propagation, mathematically represented by an equivalent deviation from the input flat wavefront, i.e. the wavefront error (WFE).

The diffraction image from a real telescope is built by the square modulus of the diffraction integral, here represented in circular coordinates $\{r, \phi\}$ and $\{\rho, \theta\}$, respectively on FP and pupil:

$$I(r, \phi) = k \left| \int \rho d\rho d\theta P(\rho, \theta) e^{-i\pi r \rho \cos(\theta - \phi)} \right|^2. \quad (1)$$

The integration domain corresponds to the pupil; for a circular aperture, $0 \leq \rho \leq 1$; $0 \leq \theta \leq 2\pi$, where ρ is the normalised radius. The constant k provides the appropriate photometric result associated to the source emission, exposure time and collecting area; other scaling factors are neglected. The pupil function $P(\rho, \theta) = e^{i\Phi(\rho, \theta)}$, depends on the phase aberration function Φ , which is usually expanded in a series of terms, e.g. the Zernike functions ϕ_n (Born and Wolf 1985):

$$\Phi(\rho, \theta) = \frac{2\pi}{\lambda} WFE = \frac{2\pi}{\lambda} \sum_n A_n \phi_n(\rho, \theta). \quad (2)$$

The WFE itself is independent from wavelength, contrarily to the pupil function, which is affected by the $2\pi/\lambda$ factor. Also, the nonlinear relationship between the set of aberration coefficients A_n and the image is put in evidence by replacement of Eq. (2) in Eqs. 1 or A2.

The non aberrated case, corresponding to $WFE = 0$, can be solved, providing an analytic representation of the diffraction image of simple systems recalled in appendix A. The form of the diffraction integral, used in Eqs. 1 and A2, leads naturally to its implementation based on FT techniques.

2.1 Discrete and Fast FT

The Discrete Fourier Transform (DFT), e.g. from Bracewell (2003), of a one-dimensional sequence $s_n = s(z_n)$ of N samples of the signal s , function of a time variable z , is:

$$S(\omega) = \sum_{n=0}^{N-1} s_n \exp(-iz_n \omega), \quad (3)$$

where ω is the pulsation, conjugated to the signal argument. The signal s is supposed to be smooth and with finite du-

ration, with N contiguous non-zero samples; this ensures proper convergence of Eq. 3. $S(\omega)$ is evaluated on a set of M points in the desired interval. Apart variable transformation, the diffraction integral in Eq. 1 actually appears as the FT of the pupil function, with the natural extension to two dimensions of Eq. 3, and the discrete numerical form required for practical computation cases. Some remarks on sampling resolution and processing time are provided in B.

In the Fast FT (FFT) algorithm, significant improvements in the computation time are achieved under the restriction (usually quite acceptable) that the signal is uniformly sampled, so that $s_n = s(nT)$, with sampling period T . The computation of all N transform values, for each ω_q , is performed as a single process, split in a hierarchical sequence of lower order FFT steps.

The diffraction integral is physically limited to the real pupil size; however, with this limitation, only two points are generated over the characteristic length of the system, which is clearly not sufficient to provide an acceptable image detail. A typical solution consists in a formal extension of the pupil domain to larger size, allowing to achieve the desired resolution, provided the pupil function P is set to zero in the external region. In practice, the real pupil must be extended to a dummy pupil M times larger, in order to force the computation of M points in the Airy radius. The idea of zero padding for specific FT computations has been applied e.g. to the packing theorem (Bracewell 2003); it is a common approach also in ray tracing packages (Zemax, Code V).

The pupil resolution must be sufficient to sample the intrinsic variation of the WFE, e.g. placing Q points over the pupil size. This generates an array of $N = M \times Q$ points mapping the dummy pupil along one dimension; notably, $(M-1)Q$ of them have zero value. This array can be mapped by DFT onto $M \times Q$ points over the FP, and the transform array covers Q times the Airy radius.

2.2 PSF construction by FT

In the PSF construction according to the above prescription, the FFT approach involves a significant amount of computation over quantities on pupil set to zero. Also, the FP region of interest (ROI) is usually not as large as implicitly computed by the FFT, because after a few Airy diameters the PSF becomes vanishingly small for most optical systems. This consideration led us to the alternative approach of direct DFT computation according to Eq. 3 (Cancelliere and Gai 2007). The key features of this strategy are:

- restriction to the physical pupil only;
- restriction to a limited FP region.

Thus, the case considered concerns the comparison between FFT applied to a square image of logical format $N \times N$, where $N = M \times Q$, and DFT applied to an input array $Q \times Q$ to generate an array $M \times M$. For convenience of some numerical examples below, we will set $M = Q$, although this is by no means a restriction to the method.

3 TEST OF FFT AND DFT

The first relevant comparison between FFT and DFT algorithms concerns their effectiveness, i.e. their capability

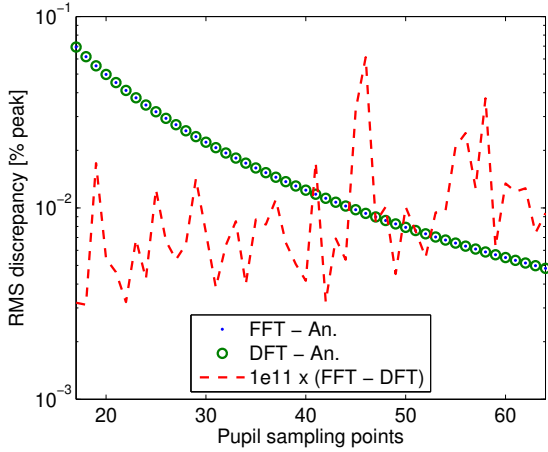


Figure 1. RMS discrepancy between FFT, DFT and analytic non aberrated PSF vs. number of sampling points.

of providing the correct result. Both are derived from the same diffraction integral, so that, apart the case of actual coding errors, they both rely on the same convergence conditions, and are expected to provide the same result, within numerical errors. The simulation is implemented on a desktop computer with a Pentium II processor, clock 2 GHz, 512 MB RAM, in the Matlab environment (<http://www.mathworks.com>). The Matlab `fft` function is based on the FFTW library (<http://www.fftw.org>), described in Frigo and Johnson (1998), which is commonly considered to be quite efficient, whereas the DFT is implemented by straightforward coding of Eq. 1 for the rectangular aperture case, as in appendix A.

3.1 Non aberrated PSF

The first test is performed on non aberrated images, since this is the only practical case in which an analytic representation of the diffraction image is readily available (appendix A). The Gaia telescope parameters are used: rectangular aperture, size $D_x = 0.5$ m times $D_y = 1.4$ m (high resolution in the y direction); focal length $F = 35$ m. The ROI on the FP is restricted to $\pm 600 \mu\text{m}$ (x) \times $\pm 200 \mu\text{m}$ (y), with resolution respectively 6 and 2 μm , and the DFT is computed only over this region, using the FFT sampling points over both pupil and FP.

The DFT or FFT precision improves with increasing resolution of the sampled function, i.e. with increasing number of points. The PSF discrepancy between the FFT and DFT result, respectively, and the analytic expression, is computed vs. increasing resolution in the pupil plane, over the range $Q = 10$ to 64 sampling points. Since the actual FFT image format is Q^4 , the largest array generated is $4K \times 4K$, i.e. 16 million pixels. At this point, our desktop computers already have a significant virtual memory usage.

The discrepancy is evaluated as mean, peak to valley (hereafter “peak for simplicity”) and RMS value of the difference between computed PSFs, evaluated on the whole ROI. The RMS discrepancy of both FFT and DFT with respect to the analytic PSF (shown in Fig. 1, respectively by dots and circles) decreases with increasing sampling resolution, as ex-

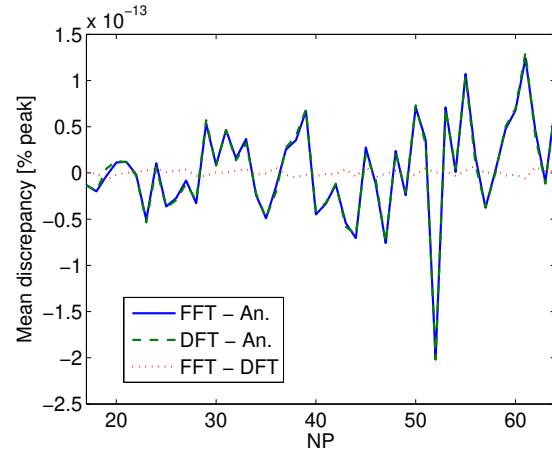


Figure 2. Mean discrepancy between FFT, DFT and analytic non aberrated PSF vs. number of sampling points.

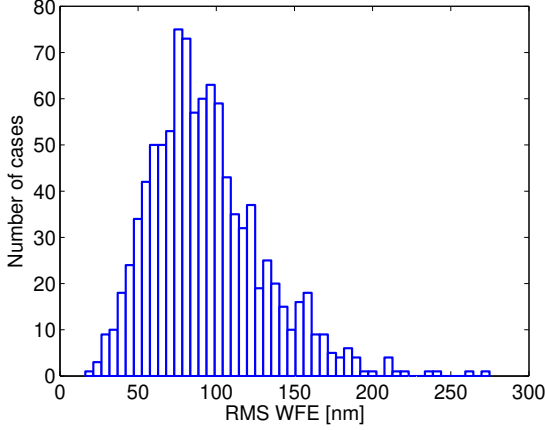
pected; also, the RMS difference between FFT and DFT (dashed line) is quite small, $\sim 1e - 15$ of the PSF peak. Since the minimum real number used (the Matlab constant “*eps*”) is $2.22e - 16$, the discrepancy between DFT and FFT results is quite close to the limiting numerical noise. Thus, both FFT and DFT compute the desired approximation to the analytic PSF, with negligible difference between them. A similar improvement with sampling resolution is shown by the peak discrepancy of FFT and DFT vs. analytic PSF; also, the mean discrepancy remains quite small (order of $1e - 15$ of the PSF peak value) over the whole range, as shown in Fig. 2. In particular, when the pupil is sampled with more than 14×14 points the RMS discrepancy over the ROI drops below 0.1% of the peak value, and the $1e - 4$ level is reached for more than 45×45 points in the pupil. Similarly, the peak discrepancy is below 1% when using more than 14×14 points and below 0.1% with sampling above 48×48 points.

3.2 Aberrated PSF

The non aberrated PSF case, although quite useful for comparison of the two FT methods, is not particularly interesting from an optical standpoint, since any real system has deviations from the ideal case. However, for a general aberrated case, an analytic representation is *not* available, so that the above simulation cannot be extended to the images related to an arbitrary case. However, we can build a set of aberrated cases and evaluate the PSF discrepancy between DFT and FFT results, which can be compared with the corresponding non aberrated case.

We generate a set of 1000 aberration cases, with sampling resolution of 24 points, using a Gaussian distribution of the Zernike coefficients with $\sigma = 100$ nm. The resulting RMS WFE distribution is shown in Fig. 3. The average value is 94 nm, i.e. an acceptable value for realistic optics in the visible ($\sim \lambda/6$ at $\lambda = 600$ nm), with standard deviation 36 nm.

For each set of aberration coefficients, the PSF is built by both FFT and DFT, then the FFT result is cut to the size of the selected FP ROI, where also the DFT is computed. The discrepancy between the two PSF versions is evaluated, deriving for each case the mean, peak and RMS

**Figure 3.** Histogram of the RMS WFE**Table 1.** Statistics of mean, peak and RMS discrepancy between DFT and FFT result, over the sample of 1000 aberration cases.

	Sample Mean	Sample RMS
ROI mean discrepancy	$5.7e-19$	$2.8e-17$
ROI peak discrepancy	$3.3e-15$	$1.9e-15$
ROI RMS discrepancy	$1.5e-16$	$1.1e-16$

values over the ROI, and recording the values for the whole the statistical sample of aberration cases.

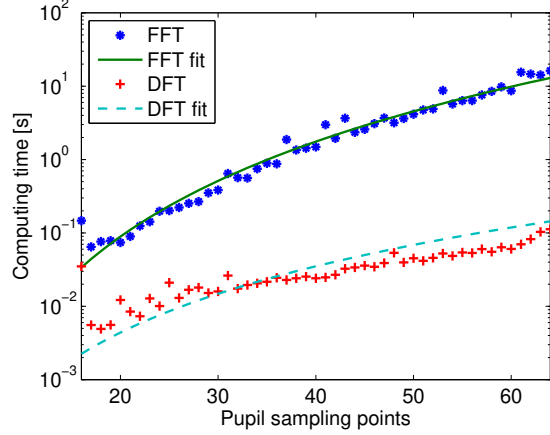
The results are shown in table 1. The PSF difference between the FFT and DFT methods, for a general case of aberration, remains quite small, comparable to their discrepancy for the non aberrated case ($\sim 1e-15$ of the peak), and compatible with the numerical noise already experienced in the previous test. Therefore, also for the general case of an arbitrary PSF, the DFT method generates a very good representation of the FFT result.

3.3 Processing time

The processing time for a one-dimensional FFT on N points is order of $N \log N$, and $\sim N^2$ for DFT. We deal with two-dimensional images of logical format $N \times N = Q^2 \times Q^2$, in which the region of interest is of order of $Q \times Q$ pixels. The FT computational load can be explicitly derived for the bi-dimensional case corresponding to PSF computation.

We consider the case in which the one-dimensional FT algorithm is repeated $N = Q^2$ times for the FFT, and Q times for the DFT, although this is not necessarily the most efficient implementation. Then, the cost for bi-dimensional FFT and DFT becomes of order of $N^2 \log N^2 = Q^4 \log Q^4 \propto Q^4 \log Q$, and $Q^2 \times Q = Q^3$, respectively. Introducing additional numerical factors (e.g. the Airy diameters in the ROI), the scaling law with respect to the number of sampling points Q does not change, apart the coefficient. The potential gain of DFT vs. FFT is thus $\sim Q \log Q$.

Notably, similar gain may be expected in other applications in which the input data or the FT results are required with high resolution only over a restricted region for both conjugate variables. We remark also that the

**Figure 4.** Processing time vs. sampling points of FFT (stars) and DFT (crosses), and corresponding fitting functions.

condition of uniform sampling is not necessarily true for any measurement, and can be sometimes inconvenient. The above estimate of processing time is valid only within the computation-limited regime, and for any real computer, at increasing size of the processed arrays, the processing becomes input/output-limited, when the physical memory is saturated and the virtual memory mechanisms start swapping data towards the mass storage devices.

A stopwatch timer function of Matlab is used to keep track of the execution time of both FFT and DFT. The simulation is repeated for 10 iterations, in order to reduce the fluctuations due to operating system overheads. The processing time is averaged over the 10 sets, providing the results shown in Fig. 4, where the fit to the analytic functions $Q^4 \log Q$ (FFT) and Q^3 (DFT), is also shown. The fit to experimental data is reasonable, although noisy; the fit parameters are respectively 129 ns (FFT) and 548 ns (DFT).

Over the range of cases considered, DFT is significantly more efficient than FFT, and the growth rate of the computational cost is lower.

4 WAVELENGTH DEPENDENCE

Since in our examples the FP resolution is fixed ($2 \mu\text{m}$), the pupil resolution scales with the wavelength λ : the pupil is better sampled at shorter wavelength and vice versa. The variable pupil resolution is potentially associated to artefacts in the images, depending on wavelength, leading to potential measurement errors, as in Busonero et al. (2006). In order to test this aspect, the wavelength range $\lambda_1 = 590 \text{ nm}$ to $\lambda_2 = 610 \text{ nm}$ is explored with $\Delta\lambda = 1 \text{ nm}$ resolution. The case considered is the non-aberrated optical PSF, because of the known analytic representation. We evaluate the discrepancy with respect to the analytical function of three different PSF representations, respectively built one by FFT, and two by DFT, the former using the FFT pupil sampling resolution (DFT 1), and the latter using fixed sampling of 64 points on the pupil (DFT 2). Notably, DFT 2 resolution is lower than FFT or DFT 1, using respectively 136 (η) and 146 (ξ) points at $\lambda = 600 \text{ nm}$.

The variation with wavelength of the three cases of PSF

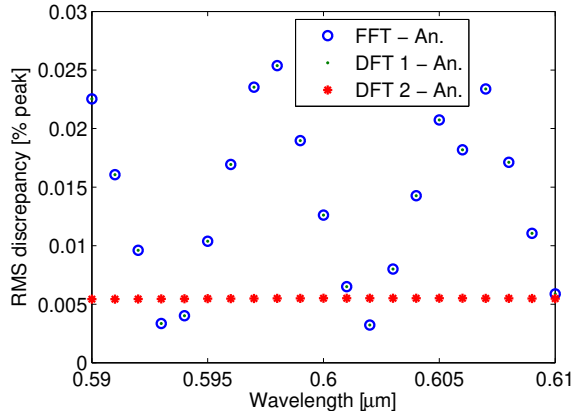


Figure 5. PSF discrepancy vs. wavelength of FFT (circles), DFT 1 (dots) and DFT 2 (stars).

discrepancy with respect to the analytic representation is shown in Fig. 5, respectively for the results from FFT (circles), DFT 1 (dots), and DFT 2 (stars). The DFT 1 resolution was chosen to match the FFT resolution, so that it is reasonable to expect similar behaviour. We remark the large variation in discrepancy of FFT and DFT 1 over a comparably narrow spectral range. This is expected to lead to potentially significant errors in the construction of polychromatic images, *depending on the selected spectral sampling*.

Besides, using a constant pupil sampling vs. wavelength (as for DFT 2, compatible with fixed FP resolution), we get a uniform distribution of PSF discrepancy vs. wavelength. In spite of lower pupil resolution, the precision of DFT 2 is significantly better over most of the wavelength range, and above all it is constant, i.e. wavelength independent.

5 EXTREMELY LARGE TELESCOPES

The next generation of telescopes currently studied aim at a significant improvement in sensitivity with respect to current instrumentation, as for the Overwhelmingly Large telescope (OWL), in Gilmozzi (2004). Of course, the related cost and engineering challenge is also significant. Other proposed Extremely Large Telescopes (ELTs) also have typical size of a few ten meters, sometimes achieved as diluted apertures, as proposed e.g. in Martin et al. (2003), for a better trade-off between complexity and sensitivity.

The PSF computation for such instruments is in principle based on the same tools (diffraction integral) used for previous telescopes. Besides, processing improvements may be appealing to the purpose of increased precision in the analysis and more efficient design development.

In recent propositions, the OWL diameter is 42 m; as an example, we assume operation in the K band ($2.2 \mu\text{m}$), corresponding to an Airy diameter of 26 milli-arcsec, and requiring an effective focal length of 560 m for its imaging on four $18 \mu\text{m}$ pixels. For simulation of the OWL PSF, we assume a minimum sampling of order of 10 points per pixel, i.e. 40 points over the Airy diameter, corresponding to $1.8 \mu\text{m}$ resolution on the focal plane. We set again the ROI size on the FP to 6 Airy diameters (on each dimension), for a logical format of 240×240 pixels.

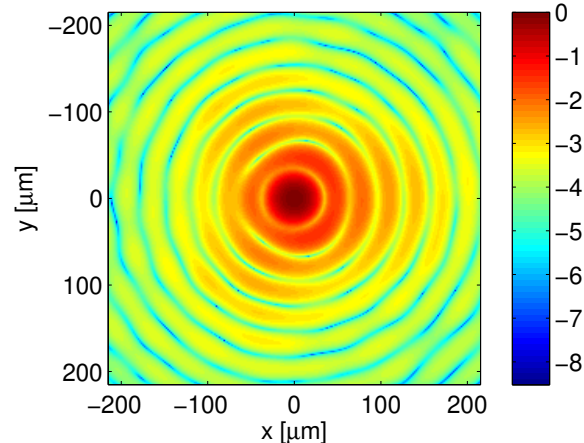


Figure 6. Example of an OWL PSF with static aberrations and AO residuals.

For proper sampling of the atmospheric turbulence over the telescope pupil, in K band, we set a resolution of order of 0.1 m, requiring an array of 420×420 points on pupil. However, the FFT size associated to the problem, due to the compound effect of 40 points in the Airy diameter times 420 points on the pupil, is 16800×16800 , simply unmanageable on the desktop class computer used in our simulation.

The simulation is set with a few Zernike coefficients set to non zero values, to mimic a realistic optical response, and with a Gaussian random residual from AO correction, with $\sigma = 300 \text{ nm}$. The corresponding RMS WFE on the pupil in the case shown is 310 nm. The resulting PSF is shown in Fig. 6, in logarithmic units; the signal profile is affected by perturbations both on low and high frequency, respectively from optical aberrations and AO residuals. The monochromatic PSF computation requires about 0.6 s, increasing to about 5 s for 0.05 m pupil resolution. Therefore, analyses of such optical system, either with respect to instrumental aspects (including AO response) or to astrophysical performance, can be done without high-end computers. Besides, for a given computing power, the proposed method allows a significant increase of the range of study cases, e.g. for statistical evaluation.

6 CONCLUSION

When PSF computation is required only on a limited region of the focal plane, DFT computation can be significantly more efficient than FFT, providing the same results (within the numerical noise) with much lower processing time. This is because computation is restricted to the actual points required by the problem, rather than those imposed by the FFT definition on both input and output variables. Both FFT and DFT produce a good PSF representation, with precision increasing with the number of sampling points used. Artefacts can be introduced in the PSF, e.g. as a function of wavelength, depending on the sampling strategy; DFT provides more flexibility and can thus improve the precision.

Processing time is relevant also with respect to preci-

sion of the PSF computation and of the performance analysis based on such data; in particular, precision is in many cases dependent on the number of sampling points used for representation of the relevant problem variables. Therefore, the capability of processing higher resolution data, in a given time frame, ensures higher precision on each PSF; besides, it is also possible to take advantage of the proposed method to improve the statistical sampling of the problem domain, by generation of a larger amount of simulated data, depending on the most convenient trade-off.

Also, the development of new generation, large size telescopes may benefit from faster and more accurate computation tools, for both design and science assessment.

ACKNOWLEDGMENT

The authors would like to thank M.G. Lattanzi, D. Busonero, and D. Loreggia for useful comments on the possible application of the proposed methods. The paper readability benefits of the referee's remarks.

REFERENCES

- Busonero D., Gai M., Gardiol D., Lattanzi M.G., Loreggia D., 2006, *A&A*, 449, 827
 Born M., Wolf E., 1985, *Principles of optics*, Pergamon, New York
 Braat J., Dirksen P., Janssen A.J.E.M., 2002, *J. Opt. Soc. Am. A*, 19, 858
 Bracewell R., 2003, *The Fourier Transform and its Applications*, McGraw-Hill, New York
 Cancelliere R., Gai M., 2006, *IEEE Trans. on Pattern Analysis and Machine Intelligence*, (submitted) MODIFY
 Frigo M., Johnson S.G., 1998, *Proc. Int. Conference on Acoustics, Speech, and Signal Processing*, 3, 1381
 Gai M., Cancelliere R., 2005, *MNRAS*, 362, 1483
 Gilmozzi R., 2004, *Proc. SPIE*, 5489, 1-10
 Martin H.M., Angel J.R.P., Burge J.H., Miller S.M., Sasian J.M., Strittmatter P.A., 2003, *Proc. SPIE*, 4840, 194
 Perryman M.A.C., de Boer K.S., Gilmore G., Høg E., Lattanzi M.G., Lindegren L., Luri X., Mignard F., Pace O., de Zeeuw P.T., 2001, *A&A*, 369, 339

APPENDIX A: IDEAL DIFFRACTION IMAGES

In the simple case of an unobstructed circular pupil of diameter D , at wavelength λ , and with focal length F , we get the radial symmetric PSF of Eq. A1:

$$I(r) = k \left[2 \frac{J_1(\pi r D / \lambda F)}{\pi r D / \lambda F} \right]^2. \quad (\text{A1})$$

Here J_1 is the Bessel function of the first kind, order one, and r the radial FP coordinate. The image characteristic size is the Airy diameter: $2.44\lambda F/D$.

For a rectangular pupil, it is convenient to use cartesian coordinates, e.g. $\{x, y\}$ on FP and $\{\xi, \eta\}$ on the pupil, with integration performed over the appropriate region:

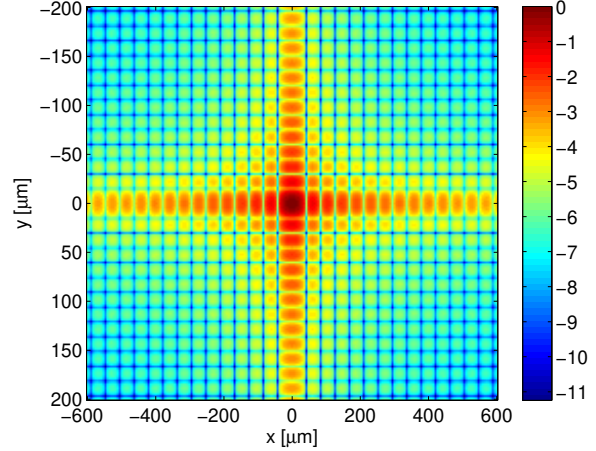


Figure A1. Non aberrated PSF of Gaia: logarithmic intensity at 600 nm.

$$I(x, y) = k \left| \int d\xi d\eta P(\xi, \eta) e^{-i\pi(x\xi + y\eta)} \right|^2. \quad (\text{A2})$$

As an example, we consider the current Gaia telescope geometry, i.e. a rectangular aperture, with size $D_x = 0.5 \text{ m} \times D_y = 1.4 \text{ m}$ (high resolution in the y direction) and focal length $F = 35 \text{ m}$. The PSF is described by the *sinc* squared function, where $\text{sinc } z = (\sin \pi z) / (\pi z)$ (Bracewell 2003):

$$I(x, y) = \text{sinc}^2\left(\frac{x D_x}{\lambda F}\right) \times \text{sinc}^2\left(\frac{y D_y}{\lambda F}\right). \quad (\text{A3})$$

A representation of the non aberrated PSF, at $\lambda = 600 \text{ nm}$, is shown in Fig. A1, in logarithmic units normalised to the central peak intensity.

APPENDIX B: FT RESOLUTION AND PROCESSING

Usually, a uniform sampling period T is assumed for DFT, although this is not strictly implicit in the definition 3. The signal transform is computed at pulsation $\omega_n = 2\pi n/(NT)$, where $n = 0 \dots (N-1)$, so the resolution is $\Delta\omega = 2\pi/(NT)$ (or $\Delta\nu = 1/(NT)$, in terms of frequency: $\omega = 2\pi\nu$). The DFT thus associates the resolution in one domain to the full range of the corresponding conjugate variable.

The computational load of FFT and DFT of a sequence of N values is respectively of order of $N \log N$ and N^2 , so that for increasing N the FFT is much more convenient of DFT performing the same computation. The expression is valid only when the number of samples is a power of two: $N = 2^n$, for some integer n ; for other values, the result is highly dependent on the selected algorithm.

The numerical implementation of the DFT for the rectangular pupil case follows from the definition, apart details of proper definition of the pupil and FP coordinates, respectively $\{x_n, y_m\}$ and $\{\xi_p, \eta_q\}$, with suitable indices $\{n, m, p, q\}$:

$$I_{nm} = I(x_n, y_m) = k \left| \sum_{p,q} P(\xi_p, \eta_q) e^{-i\pi(x_n \xi_p + y_m \eta_q)} \right|^2. \quad (\text{B1})$$